PHYSICAL REVIEW A VOLUME 52, NUMBER 6 DECEMBER 1995

Electron-impact core excitation of SF_6. II. Generalized oscillator strengths in the S 2*p* region

Cássia C. Turci,[1,2] James T. Francis,[1] Tolek Tyliszczak,[1] G. Gerson B. de Souza,[2] and Adam P. Hitchcock[1]
[1]*Department of Chemistry, McMaster University, Hamilton, Ontario, Canada L8S 4M1*
[2]*Instituto de Quimica, Universidade Federal do Rio de Janeiro, 21910-900 Rio de Janeiro, Brazil*

(Received 7 April 1995)

The generalized oscillator strengths (GOSs) for discrete and continuum S 2*p* excitations of SF_6 have been derived in the momentum transfer range (K^2) of 1–20 a.u.$^{-2}$ from the angular variation of the relative differential cross section for inelastic electron scattering. The experimental techniques and data processing procedures used to obtain reliable, absolute GOS values are documented. The GOS results are compared to recent literature results [J. F. Ying, C. P. Mathers, and K. T. Leung, Phys. Rev. A **47**, R5 (1993)]. Some discrepancies are noted. These are found to arise largely, but not completely, from differences in the data analysis procedures used. The Bethe surface for SF_6 in the region of S 2*p* excitation is derived and the important role of Compton scattering by valence electrons is illustrated.

PACS number(s): 34.80.Gs, 33.20.Rm, 33.70.Ca

I. INTRODUCTION

Electron energy-loss spectroscopy (EELS) has been used extensively for core excitation spectroscopy, both at low and high resolution. A bibliography of atomic and molecular inner-shell excitation studies has been published recently [2]. EELS can be used to study both electric-dipole transitions, which are detected in optical studies, and nondipole (electric-quadrupole, spin-exchange) interactions, which normally are not detected by one-photon optical spectroscopies. Part I of this work [3] compared dipole and nondipole electron energy-loss spectra of SF_6 in the S 2*p*, S 2*s*, and F 1*s* regions. References to earlier studies of the core excitation spectroscopy of SF_6 were provided in paper I and will not be repeated here.

This paper presents the results of a quantitative analysis of the S 2*p* EELS intensities. The concept of generalized oscillator strength (GOS) for electron scattering, which was introduced by Bethe [4] and discussed in detail by Inokuti [5], provides a very useful framework for quantitative analysis of EELS intensities. Bethe [4], using the first Born approximation, showed that there was a quantitative relationship between the differential cross section for fast inelastic electron scattering and the generalized oscillator strength $f_{on}(K)$:

$$f_{on}(K)=(E_{on}k_0K^2/2k_n)(d\sigma_{on}/d\Omega), \tag{1}$$

where $\mathbf{k}_0$, $\mathbf{k}_n$, and $\mathbf{K}$ are the incident, scattered, and transferred momenta, E_{on} is the energy-loss for the $|o\rangle\rightarrow|n\rangle$ transition, and $d\sigma_{on}/d\Omega$ is the measured differential scattering cross section, which is the strength of inelastic scattering of an incident beam of energy E_0 into solid angle $d\Omega$ over the energy-loss interval.

Bethe also showed that the generalized oscillator strength can be expanded in a power series of K^2 as

$$f_{on}(K)=f_0+AK^2+BK^4+\cdots, \tag{2}$$

where f_0 is the optical oscillator strength (OOS) containing the electric-dipole matrix element (ϵ_1); $A=\epsilon_2^2-2\epsilon_1\epsilon_3$, where ϵ_2 is the quadrupole and ϵ_3 is the octupole matrix element; $B=\epsilon_3^2-2\epsilon_2\epsilon_4+2\epsilon_1\epsilon_5$ contains higher-order electric-multipole terms, etc.

In the limit of zero momentum transfer (infinitely high incident energies and scattering angle of 0°) the generalized oscillator strength becomes equal to the optical oscillator strength f_0. The OOS cannot be measured directly by electron-impact spectroscopy since there is always some minimum nonzero momentum transfer in the inelastic collision due to the finite impact energy and finite range of scattering angles. However, values of K^2 can often be achieved that are sufficiently small that the GOS is indistinguishable from the OOS [6]. Chan *et al.* [7–9] have obtained accurate optical oscillator strengths for transitions in noble gases using extremely small scattering angles and very high impact energies relative to energy loss. Alternatively accurate determination of the OOS can be obtained by measuring the GOS in the small-K^2 region and extrapolating to $K^2=0$ [10–13]. Lassettre and co-workers [12,13] have derived absolute OOS functions for valence excitations of a large number of molecules by extrapolation of the GOS to $K^2=0$. Recently, Msezane and Sakmar [14] have derived a universal formula to extrapolate GOS data to $K^2=0$ and have shown that their procedure produces results in excellent agreement with experimental measurements for $K^2\leqslant 0.05$ a.u.$^{-2}$.

Conversely, in the region of large momentum transfer, optically forbidden transitions can be excited. Several nondipole transitions have been identified from *K*-dependent studies [15–20]. In addition to the spectroscopic detection of states which are inaccessible by dipole excitation, studies of the GOS for nondipole excitations can provide useful information with regard to spectral assignments. First, the relative importance of impact energy versus angular variation of spectral intensities can distinguish various classes of nondipole processes. Spin-exchange transitions are excited when the impact energy approaches the excitation threshold [21], whereas quadrupole (and higher-order electric-multipole) excitations are most enhanced by large scattering angles at moderate impact energies. Second, the K^2 variation of the GOS may provide qualitative information about spectral assignment. Bonham [22] and Kim *et al.* [23] have explained the origin of GOS minima observed in the Rydberg states of atoms. It has been proposed that low-lying Rydberg states of molecules are also characterized by a minimum in the GOS as a function of momentum transfer [24–26]. A common configurational origin of two states may be indicated by the similarity in shape of their GOS. This appears to be the case for the GOS of the 177- and 181-eV nondipole excitations, which we have attributed primarily to states arising from the (S $2p^{-1}, t_{1u}$) configuration [3]. Third, absolute GOS measurements provide an additional tool with which to assess the relative accuracy of different quantum chemical calculations. If GOS calculations are available, a comparison of the shape as well the absolute magnitude of calculated and experimental GOS profiles can help both in the evaluation of computational procedures and in determining correct spectral assignments [20,27,28].

The generalized oscillator strengths can be visualized in the form of the Bethe surface [5], a three-dimensional representation of the GOS as a function of energy loss, and the logarithm of the momentum transfer. Shell-specific Compton profiles can be derived from the GOS measurements [29–31]. Bonham and Wellenstein [32] have shown how one can analyze the Compton profile in Bethe surfaces to determine the charge and momentum distributions of the valence-shell electron densities of atoms and molecules.

Even though the potential of EELS to provide additional spectroscopic information has been known for years, there has been little examination of nondipole *core-excited* states and relatively few systematic measurements of the GOS for valence-shell [20,27,33–40], and particularly inner-shell [1,41–45], excitation. One of the latter studies is that of Ying, Mathers, and Leung [1], who have recently reported GOS curves for four S $2p$ excited states of SF_6.

We have used angle-resolved electron energy-loss measurements to determine the GOS of SF_6 in the region of S $2p$ excitation and ionization. Since this is the first quantitative GOS measurements with our apparatus, we provide a detailed evaluation of our acquisition and analysis procedures for obtaining reliable EELS intensity data and its conversion to absolute GOS values. We compare our GOS curves for specific S $2p$ excited states and resonances to those reported in the literature [1]. There are significant discrepancies in the GOS of several states. A detailed comparison of the data analysis procedures used in the two experiments sheds light on the source of these discrepancies. The Bethe surface in the region of S $2p$ excitation is generated. Comparison of the GOS with the as-measured data provides a good illustration of the dominant role of the Bethe ridge (Compton scattering from the valence electrons) in the region of inner-shell excitation.

II. EXPERIMENT

A. Experimental measurements

The electron energy-loss spectra of SF_6 were measured using a variable impact energy, variable angle, electron energy-loss spectrometer whose design and operation will be discussed in detail elsewhere [46]. Briefly, a gas jet is crossed by a monochromatic incident electron beam. Electrons inelastically scattered at a mechanically determined scattering angle (−10° to 110°) are dispersed using a lens system and a hemispherical electron energy analyzer. The signal is detected using a channel electron multiplier and standard pulse counting electronics. The sulfur hexafluoride (99.99% purity) used in these experiments was purchased from Matheson. It was used without further purification.

The GOS for a specific energy loss can be determined in a variety of different ways. The approach that was used as the principal method consisted of recording full energy-loss spectra (155-212 eV) at a series of different angles, extracting peak areas, and correlating all relevant factors among the separate measurements. This procedure took several months for acquiring data of adequate quality and thus we were concerned about the stability and precision of measurement of beam current, pressure, detection sensitivity, etc. In order to have an independent check on these results we measured the angle-dependent signals at a small number of selected energy losses by rapidly and repetitively scanning the scattering angle in order to derive a relative scattering cross-section curve for a single state. Relative GOS curves for the S $2p$ excited states were then derived by correcting for appropriate factors (e.g., nonjet signal; see below) and normalizing to intensities derived from full spectra recorded at a small number of scattering angles. Although both methods were used in our study, this paper is primarily based on results obtained with the first type of measurement.

S $2p$ spectra of SF_6 were acquired in six multiple measurement blocks, each of which covered a number of different scattering angles in the range 1°–25°. An impact energy (E_0) of 1400 eV was used. The angles within the measurement blocks were chosen with overlap to allow cross referencing.

During each cycle of EELS measurements the sample pressure was chosen to be as high as possible to achieve the best average count rate, but not so high as to lead to contributions from plural scattering (core plus valence loss in different scattering events). The chamber pressure was increased from a base pressure of 2×10^{-7} Torr to 2×10^{-5} Torr during measurements. In order to correct the measured signal for angle-dependent variations in the volume sampled we have measured spectra at each angle with the gas introduced at a point far from the jet interaction region. Figure 1 plots the ratio $I_{\text{total}}/(I_{\text{total}}-I_{\text{nonjet}})$ versus $\theta°$. $I_{\text{total}}=I_{\text{jet}}+I_{\text{nonjet}}$ is the signal measured when the SF_6 is introduced through a capillary doser to form a jet. This signal includes not only that from the enhanced density region of the jet but also the signal from regions in the intersection of the analyzer viewing cone and the incident beam, which are not in the jet (see the inset to Fig. 2). I_{nonjet} corresponds to the signal measured when the SF_6 gas is introduced at a point far from the interaction region at a flow rate that produced a chamber pressure identical to that used for gas jet conditions. There is an estimated 13-fold enhancement of the gas density in the portion of the gas jet, which is the collision region. This enhancement factor was obtained from the asymptotic value of $I_{\text{total}}/I_{\text{nonjet}}$ intensity ratio at large angles (Fig. 1). The data in Fig. 1 were used to correct the measured spectra to a constant interaction volume by subtracting the contribution of the nonjet gas, as explained in Sec. II B and II D. Two curves are plotted in Fig. 1, in addition to the experimental data. The inverse sinusoidal function is the expression ex-

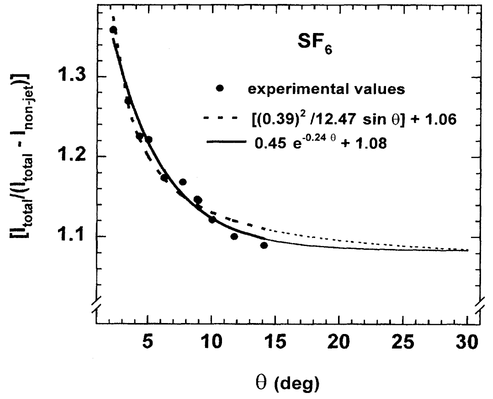

FIG. 1. Scattering angle dependence of the ratio of $I_{\mathrm{total}}/I_{\mathrm{total}}-I_{\mathrm{nonjet}}$, where $I_{\mathrm{total}}=I_{\mathrm{jet}}+I_{\mathrm{nonjet}}$ is the signal when the gas is introduced through the capillary array to form a jet away from the collision region, while I_{nonjet} is the signal measured when the gas is introduced to the same total chamber pressure at point far from the capillary. The signals are the integrated intensity between 152 and 170 eV in the two measurements. See the inset to Fig. 2 for a graphical explanation of why this ratio is a strong function of angle. See the text with regard to the fitted functions. The bold curves are fits to the experimental values, while the lighter sections of the curves are the values extrapolated to larger angles.

pected from a geometric analysis of the angle dependence of the overlap region (see Fig. 2) [46,47]. While this expression has a well-defined physical model and gave a good fit to the angle dependence of the size of the interaction region for He valence-shell measurements [46], it does not fit the SF$_6$ data as well as an empirical exponential function. The latter was used in extrapolating the correction to angles above 15° where the nonjet signal was not measured.

The spectra reported in this paper are sums of a number of individual spectra, each of which was signal averaged in both energy loss and angle for several hours acquisition. At large angles (greater than 10°) the peak count rates were only a few cps. For each angle in a measurement block, a spectrum is obtained by signal averaging until the total number of counts acquired (at all energy losses) reached a predetermined value. Because of the very rapid falloff in the cross section with increasing scattering angle, this approach often resulted in as much as a factor of 10 longer acquisition period for large-angle spectra relative to small-angle spectra. The whole measurement block was cycled several times to average out fluctuations in incident beam current, gas pressure, etc. The measurement angles were chosen to give a suitable spacing of points in K^2 space.

The instrumental energy resolution at the chosen monochromator and analyzer pass energies of 70 eV was 0.5 eV full width at half maximum (FWHM). There was some degradation of this resolution during the long acquisition periods required at large scattering angles. The reproducibility of unidirectional angle setting was $\pm 0.1°$. The accuracy was better than 1% up to 30°, as determined by mechanical measurement.

B. Data processing for quantitative GOS determination

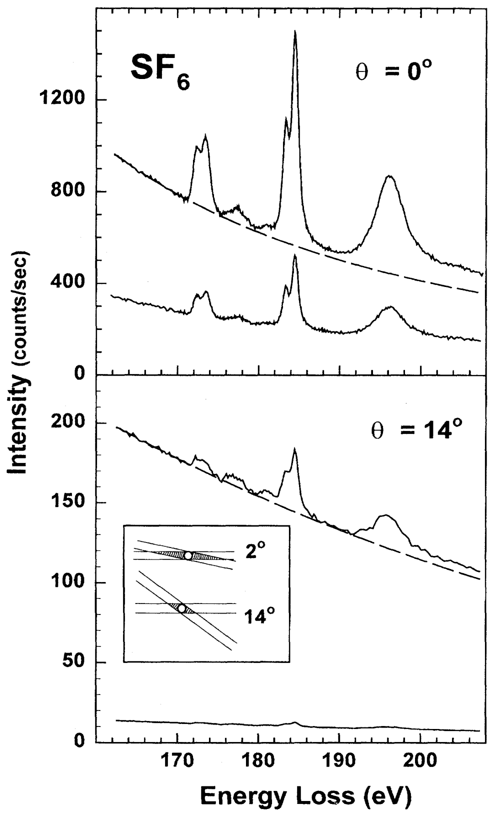

FIG. 2. S 2p EELS spectra of SF$_6$ recorded with 1400 eV impact energy and scattering angles of 0° and 14°. The upper curve in each panel is recorded with gas introduced through a capillary array (I_{total}) while the lower curve is that recorded with the gas introduced far from the interaction region to the same total chamber pressure (I_{nonjet}). The cartoon inset depicts the rapid variation of the size of the interaction region with scattering angle. Subtraction of the nonjet signal from I_{total} corrects for the angle variation in the contribution from the shaded area.

Figure 2 compares S 2p spectra of SF$_6$ recorded at forward scattering ($0° \pm 0.5°$) and at a large (14°) scattering angle, in each case with the gas introduced through the capillary ($I_{\mathrm{jet}}+I_{\mathrm{nonjet}}$) and elsewhere ($I_{\mathrm{nonjet}}$). The more intense signal of each pair of curves corresponds to gas being introduced through the capillary doser; the less intense curve corresponds to gas being introduced far from the gas jet at a rate that achieves the same chamber pressure. The count rates have been corrected for differences in beam current. The dashed lines indicate the fitted curves used to subtract the valence ionizational signal. Ideally, the intersection of the incident electron beam, the viewing cone of the analyzer, and the gas target should be identical at all scattering angles. In fact, this is not the case: at small angles the scattering volume sampled is much larger than at large scattering angles (see the inset to Fig. 2). In order to obtain a signal corresponding to a sample volume that is identical at all scattering angles, we have measured and subtracted the nonjet component at each angle. After any differences in beam current and acquisition time are taken into account, the difference in these two signals is I_{jet}, the signal from the enhanced density region of the jet. Such measurements were made for each scattering angle as shown in Fig. 1. This background correction strategy ensures that the influence of the gas on the

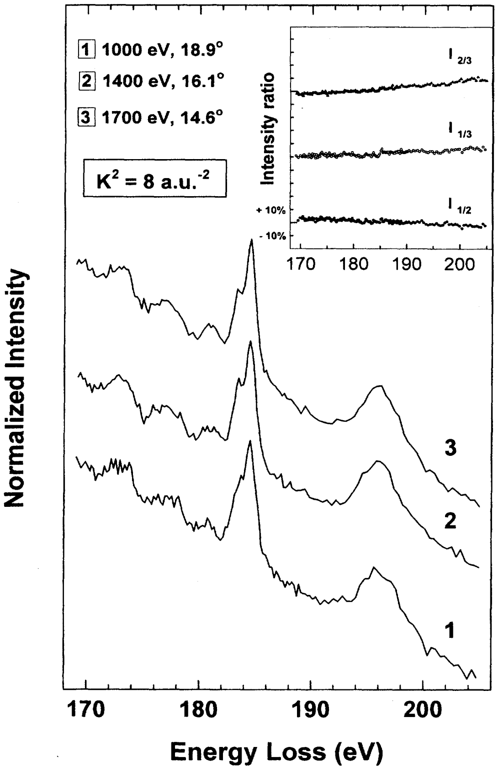

FIG. 3. Comparison of S $2p$ spectra for $K^2=8$ a.u.$^{-2}$ and impact energies of 1000, 1400, and 1700 eV. The inset shows the three pairs of ratios of these curves. The absence of spectral structure in these ratio curves indicates that the spectral shape is independent of impact energy over this range, consistent with validity of the first Born approximation.

electron gun and the electron optical surfaces remains the same since the main difference between the "jet" and "nonjet" measurements is the gas distribution in the chamber at the position of the jet. At large angles ($\theta > 15°$) the nonjet signal was assumed to be $\sim 7.5\%$ of the total, consistent with the asymptotic value in Fig. 1.

In order to make a valid GOS measurement the impact energy must be sufficiently large that the first Born approximation (and thus the Bethe-Born GOS analysis) is valid. This may be tested by checking that the GOS is independent of impact energy. Figure 3 plots S $2p$ spectra of SF_6 measured at (E_0, θ) values of 1000 eV, 18.9°; 1400 eV, 16.1°; and 1700 eV, 14.6°, in each case conditions where $K^2=8$ a.u.$^{-2}$. All three spectra were found to have the same overall shape in terms of relative intensities of individual S $2p$ peaks, which is demonstrated by the constancy of the ratio of all pairs of these three curves (see the inset to Fig. 3). The independence of the spectral shape on K is direct evidence that the first Born approximation and thus the GOS concept is valid [48] at the 1400 eV impact energy used for these measurements.

The signal corresponding solely to S $2p$ excitation and ionization was isolated from the underlying valence-shell ionization continuum by subtracting a smooth curve determined from a curve fit of the function $a(E-b)^c$ to the signal between 154 and 170 eV, below the S $2p \rightarrow a_{1g}$ peak. This is an important step since the relative amounts of underlying valence continuum change greatly with changing scattering angle, due to the valence Compton signal [29]; (see Sec. III C below). For the S $2p$ region, the maximum intensity of the Compton profile occurs around $K^2=8$ a.u.$^{-2}$. In addition, at large scattering angles where the signal is extremely weak, it is possible there are small non-gas-scattering contributions to the background from electronic noise and radioactivity or cosmic ray background.

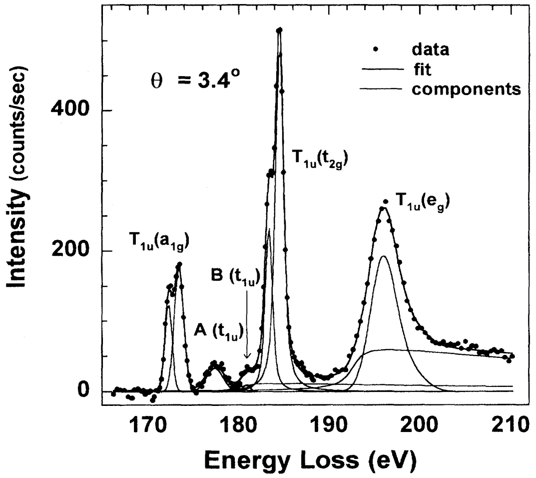

FIG. 4. Fit to the S $2p$ spectrum recorded at 3.4°, using the standardized, multifile curve-fit approach described in the text. The dark line through the data points is the result of a least-squares fit, with each peak (light line) fit to either Gaussians or a Voigt functions. Two arctangent functions are included to represent the S $2p$ continua. The asymmetric line used for the $T_{1u}(e_g)$ signal is the sum of three Gaussians of fixed relative amplitude and position. See Table I for numerical results of the constrained multiple file fit.

C. Spectral analysis

After removal of the nonjet and the valence ionization signal, the set of angle-dependent S $2p$ spectral components were then subjected to an extensive curve-fit analysis. In order to obtain the maximum physical significance and be least susceptible to curve-fitting variations associated with noise, all 18 files were fit simultaneously using a constrained optimization procedure [49]. The model for the S $2p$ spectrum consisted of a combination of Gaussian and Lorentzian peak shapes and two arctangent edge functions, chosen to match the spectral interpretation [3,50]. A simultaneous multifile analysis [49] was used to ensure that all spectra were fit with the same model. All parameters were optimized over the full set of energy-loss spectra, although only the peak and continuum amplitudes were allowed to vary independently from spectrum to spectrum.

A sample result from the curve fit is presented in Fig. 4. Numerical values from the optimized fit are presented in Table I. These values, along with a consideration of alternative, less successful fits, provide additional information about the S $2p$ spectroscopy of SF_6. The $T_{1u}(a_{1g})$ spin-orbit doublet was fit by a pair of Gaussian lines with optimized widths of 0.92 and 1.22 eV FWHM for the $[(\mathrm{S}\ 2p_{3/2})^{-1}, a_{1g}]$ and $[(\mathrm{S}\ 2p_{1/2})^{-1}, a_{1g}]$ states, respectively. Attempts to fit this band with a pair of Voigt functions based on reasonable val-

TABLE I. Energies, widths, and line shapes derived from a constrained multiple file curve-fit analysis of the S $2p$ spectra of SF_6.

	This work					Optical spectroscopy [a]				
			Width (eV)					Width (eV)		
State	E (eV)	Line type	G [c]	L [d]	Width [b]	E (eV)	Line type	G [c]	L [d]	Width [b]
$T_{1u}(a_{1g})$-3/2	172.28	Gaussian	0.92		0.92	172.27	Gaussian	0.87		0.87
$T_{1u}(a_{1g})$-1/2	173.43	Gaussian	1.22		1.22	173.44	Gaussian	1.06		1.06
A [e] (t_{1u})	177.41	Gaussian	2.14		2.14					
continuum 1	180.26	arctangent	2.52							
B [e] (t_{1u})	180.91	Gaussian	0.91		0.91					
$T_{1u}(t_{2g})$-3/2	183.37	Voigt	0.66	0.62	1.08	183.40	Voigt	0.27	0.69	0.76
$T_{1u}(t_{2g})$-1/2	184.54	Voigt	0.66	0.79	1.08	184.57	Voigt	0.27	0.78	0.85
continuum 2	192.71	arctangent	2.52							
$T_{1u}(e_g)$	195.93	Gaussian	3.19 [f]		4.1	196.2	Voigt	?[g]	?[g]	4.1
	197.93	Gaussian	3.19 [f]							
	199.93	Gaussian	3.19 [f]							

[a] From [50].

[b] Widths considering that only Gaussian line types were used for the curve fit.

[c] Gaussian contribution.

[d] Lorentzian contribution.

[e] States are labeled A and B to reflect uncertainty in assignment [3].

[f] Required to have the same value.

[g] Gaussian and Lorentzian contributions were not specified in [50].

ues of the Lorentzian natural linewidth were unsuccessful, as found in the curve-fit analysis of the photoabsorption spectrum recently reported by Hudson *et al.* [50]. As these authors have explained, this indicates inhomogeneous line broadening, associated with unresolved vibrational structure.

The $T_{1u}(t_{2g})$ spin-orbit doublet (182–188 eV) was fit using Voigt functions that had significant Lorentzian contributions. A good fit to the data was obtained using a Gaussian width of 0.66 eV FWHM and Lorentzian widths of 0.62 and 0.79 eV for the $[(\mathrm{S}\ 2p_{3/2})^{-1},t_{2g}]$ and $[(\mathrm{S}\ 2p_{1/2})^{-1},t_{2g}]$ states, respectively. The width of the Gaussian component we observe (0.66 eV) is much larger than that in the optical spectrum (0.27 eV [50]) on account of poorer experimental resolution. In both the EELS and optical work it is clear there are contributions from unresolved vibrational excitation that cause inhomogeneous broadening.

As found in the high-resolution optical study [50], spin-orbit splitting was not resolved for the electronic transition to the $(\mathrm{S}\ 2p^{-1},t_{1u})$ state at 177 eV. We do detect structure in the 181-eV nondipole signal (see Fig. 4 of [3]), but the main components are too closely spaced to arise from the spin-orbit splitting of a single state and thus we deduce the 181-eV signal arises from overlap of the spin-orbit and possibly Jahn-Teller splitting of at least two electronic transitions. The fine details of the 181-eV line shape were not incorporated into the curve-fit analysis used for GOS determination on account of the weakness of this signal at all scattering angles. Instead, only one Gaussian line profile was used to fit each of the 177- and 181-eV (t_{1u}-related) states, with optimized widths of 2.14 and 0.91 eV, respectively.

The broad asymmetric line shape of the $T_{1u}(e_g)$ (191–202) resonance was taken into account by using the sum of three Gaussian lines that were constrained to have the same width (3.19 eV) and same interline spacing (2.0 eV). Various sources of asymmetry in continuum resonances have been documented and discussed by Stöhr [51]. In this case the asymmetry is most likely associated with a decrease in resonance lifetime (and thus increase in natural linewidth) as the photoelectron energy increases across the resonance. In the multiple-scattering model this corresponds to a reduced probability of the photoelectron being trapped by the barrier at higher kinetic energy. This leads to a tailing of the resonance profile toward higher excitation energies.

In addition to the peak line shapes, two arctangent edge shapes, positioned at 180.3 and 192.7 eV, were used to account for the S $2p$ ionization continuum signal. While probably not strictly correct, a plausible interpretation is that continuum 1 is the "tunneled," below-barrier ionization and continuum 2 is the direct, above-barrier ionization (see Fig. 1 of paper I [3]). While there are momentum transfer values where only a single continuum suffices, in order to have a consistent explanation of the spectra over the whole data set, two arctangent continua were required. The edge positions and widths were constrained to be identical over the whole set. The width of the arctangent continuum onset is 2.52 eV for both continuum 1 and continuum 2. In principle, this width should reflect the lifetime broadening of the S $2p$ ionized states, with perhaps an additional contribution from vibrational excitation. In practice, the fitted width is considerably broader, perhaps in order to mimic the slow turn-on of S $2p$ ionization, which is characteristically peaking several eV above the ionization threshold. Although the analysis of these continuum steps is not without ambiguity, it is very important to include them in the curve-fit analysis since they affect the position and area of peaks in their proximity. This is one factor in the difference between our results and those previously reported [1].

D. Absolute GOS and error treatment

From the Bethe-Born relation [Eq. (1)], the following approximate expression can be derived, which was used to extract the absolute GOS from the measured data:

TABLE II. Optical oscillator strengths for S $2p$ excitations of SF_6.

	EELS GOS extrapolated to $K^2=0$			Optical	
State (UMO)	This work [a]	This work [b]	Ying *et al.* [c]	Dehmer [d]	Belchschmidt *et al.* [e]
$T_{1u}(a_{1g})$	0.079(8)	0.081(8)	0.033	0.096	0.087
A [f] (t_{1u})	0.0085(8)	0.006(2)	0.0042		
B [f] (t_{1u})	0.0006(3)				
$T_{1u}(t_{2g})$	0.23(2)	0.22(2)	0.103	0.23	0.18
$T_{1u}(e_g)$	0.20(2)	0.20(2)	0.065	0.34[g]	0.24[g]

[a] Based on Lassettre series. Errors (precision) estimated as 10%, except for the 177-eV signal.

[b] Graphic extrapolation.

[c] Reference [1]. Based on Lassettre series from the absolute GOS (eV^{-1}) derived from peak heights. Units are in eV^{-1}.

[d] Reference [52].

[e] Reference [53].

[f] States are labeled A and B to reflect uncertainty in assignments [3].

[g] Difficult to determine due to a continua contribution.

$$f(K)=N(E/2)[E_0/(E_0-E)]^{1/2}K^2\int[(I/ipt)_j-(I/ipt)_b-I_{fvb}]dE, \tag{3}$$

where N is the scale factor for setting the absolute GOS; E is the energy loss; E_0 is the impact energy; K^2 is the momentum transfer, where $K^2=k_0^2+k_n^2-2k_nk_1\cos\theta$, with $k_0^2=(2E_0/27.21)$ and $k_n^2=[2(E_0-E)/27.21]$ in a.u.; I is the accumulated intensity: $j=I_{\text{total}}$, $b=I_{\text{nonjet}}$; i is the electron-beam current; p is the gas pressure; t is the spectral accumulation time [(number of scans)×(time per scan)]; I_{fvb} is the fitted valence ionization continuum background; and $\int dE$ is integration over a fitted peak. Excluding N, the quantity in front of the integral sign in Eq. (3) is the kinematic correction factor. It should be noted that for each angle, K^2 was assumed to be constant since it changes very little over the energy range of the S $2p$ electronic transitions. The integral yields the corrected areas of the inelastic peak profiles at each scattering angle, as explained in Sec. II B. These areas correspond to the integrated differential cross sections.

The scale factor (N), which is used to convert the relative to the absolute GOS was determined by extrapolating the GOS values for the a_{1g} and t_{2g} features to $K^2=0$ and then deriving N from the match of these relative OOSs to absolute OOSs derived from the literature [52,53] (see Table II). S $2p$-isolated OOSs were not reported in these articles, so they were derived by digitization, background subtraction, and integration. There are relatively large differences in the literature OOS values (see Table II), which is a significant source of uncertainty in our absolute results. The values presented by Dehmer [52] are approximately 30% higher for t_{2g} and 9% higher for a_{1g} than those reported by Blechschmidt *et al.* [53]. Addison-Jones *et al.* [54] have also determined the S $2p$ photoabsorption cross sections of SF_6. These values range from a background of 4.6 Mb due to valence ionization to 8.4 Mb at the maximum of the t_{2g} resonance, a value that is only half that reported by Dehmer (16 Mb [52]). Addison-Jones *et al.* [54] were puzzled by this result. They suggested that this difference could be due in part to nonideal gas behavior. Another possible factor could be absorption saturation effects. We have not used their values in our work.

The relative errors in our GOS values are estimated considering the sum of the uncertainties in the momentum transfer (K^2), the integrated peak area, and the normalization factor (N). The error associated with K^2 is determined from the uncertainty in the scattering angle, taken to be 0.25°. Since this fixed angular error is increasingly important at low scattering angles, the error in K at low K^2 is much larger than that at high K^2. Since the value of K^2 is incorporated into the GOS conversion [see Eq. (1)], this gives rise to larger error bars for the GOS at small K^2 values even though the signal strength is more than an order of magnitude greater than at large K^2 and thus the error from counting statistics is much less. The error associated with the determination of peak areas includes contributions from the normalization to the gas pressure and the incident beam current. Besides these, there are contributions from the statistical precision of the data and the fitting model. All of these factors are treated as uncorrelated quantities and are added in quadrature to give the total error in the peak area. The error we have chosen to associate with N is the standard deviation of the values determined from different literature optical values. The total error in the GOS at each angle (K^2 value) was then determined by a quadrature addition of the uncertainties in K^2, peak area, and N. This procedure was carried out for each feature to give the errors bars shown in Figs. 5 and 6.

III. RESULTS AND DISCUSSION

A. GOS curves

The GOSs in the K^2 range from 0.6 to 19 a.u.$^{-2}$ for the three dipole-allowed transitions are presented in Fig. 5. Figure 6 presents the GOS results for the two quadrupole states, which are labeled only as A and B on account of some uncertainty in their correct assignment [3]. The Lassettre series [10,11,13,55] which is valid when the Born approximation holds, is a systematic way of deducing parameters related to the multipole transition matrix elements from experimental GOS data. The data in Figs. 5 and 6 were fit using a least-squares procedure to the following polynomial, which is a slightly modified form of the Lassetre series:

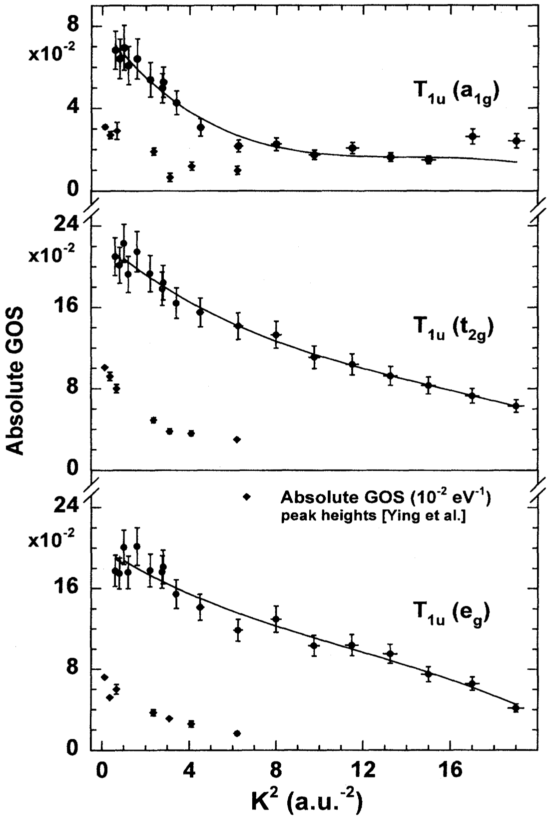

FIG. 5. GOS curves for the $T_{1u}(a_{1g})$, $T_{1u}(t_{2g})$, and $T_{1u}(e_g)$ dipole-coupled S $2p$ excited states derived from the experimental data as described in the text. The solid lines indicate the fitting to the Lassettre series expression using the parameters indicated in Table III. The solid lozenge symbols are the peak-intensity-based GOS values reported by Ying, Mathers, and Leung [1].

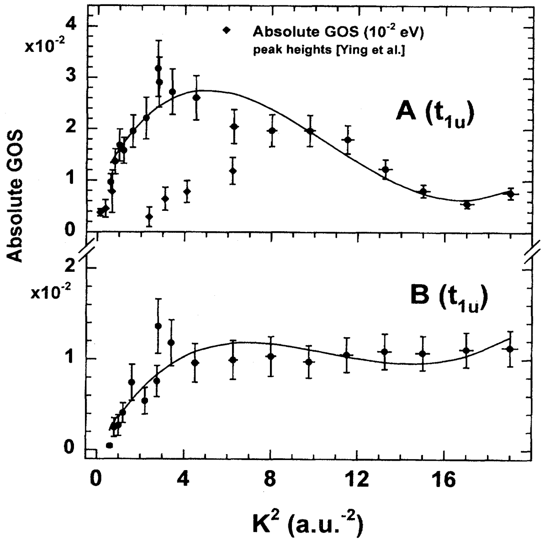

FIG. 6. GOS curves for the $A(t_{1u})$ (177 eV) and $B(t_{1u})$ (181 eV) quadrupole-coupled S $2p$ excited states. Note that the $A(t_{1u})$ signal include some contribution from unresolved Rydberg states, but this is relatively small, except at low momentum transfer. The solid lines indicate the fitting to the Lassettre series expression using the parameters indicated in Table 3. The solid lozenge symbols for the $A(t_{1u})$ signal are the peak-intensity-based GOS values reported by Ying, Mathers, and Leung [1].

$$f=[1/(1+X)^6]\{f_0+f_1[X/(1+X)]+f_2[X/(1+X)]^2+\cdots +f_m[X/(1+X)]^m\}, \qquad (4)$$

where $X=K^2/\alpha^2$, $\alpha=(2I)^{1/2}+(2|I-W|)^{1/2}$, I is the S $2p$ ionization potential of the molecule (taken to be 181.0 eV, the average values for the $2p_{3/2}$ and $2p_{1/2}$ ionization values [56,57]), and W is the excitation energy of the transition. While the regular Lassettre series uses the signed term value $(I-W)$, Eq. (4) uses the absolute value of this number to allow analysis of the t_{2g} and e_g transitions, which are above the S $2p$ edge.

A good fit of the Lassettre formula to the data for all features was obtained when only four terms were used [$m=3$ in Eq. (4)]. The resulting coefficients are shown in Table III. The value of the optical oscillator strength (f_0) is the GOS extrapolated to zero momentum transfer. The higher-order f_n terms are related to linear combinations of the respective multipole matrix elements. Although the higher-order coefficients are sensitive to small changes in the data, they were found necessary to reproduce the data smoothly.

The dipole-allowed transitions exhibit negative values for f_1 and f_3 and positive values for f_2. Opposite signs for the same quantities were found for the dipole-forbidden transitions. As discussed in the literature [1,13,58], the behavior of these coefficients (relative magnitudes and signs) can help to qualitatively infer if a particular excitation is dominated by a dipole or nondipole interaction. For instance, positive f_1 and small f_0 values are good indications of quadrupole transitions [1,13,20,59]. Table III compares the values derived from the Lassettre series analysis of our results (using both peak-area and peak-height-based GOSs) with those reported by Ying, Mathers, and Leung [1]. While there are similar trends in the sign and relative magnitudes of the terms, our f_0 values based on peak areas are typically twice as large as those of Ying, Mathers, and Leung. This largely reflects the fact that Ying, Mathers, and Leung used peak heights rather than peak areas in their GOS determination. This factor and other reasons for discrepancies in GOS values are outlined below.

Figures 5 and 6 demonstrate that dipole-allowed and dipole-forbidden transitions have qualitatively different GOSs. In particular, the GOSs for the three dipole-allowed transitions [S $2p(2t_{1u})\rightarrow 6a_{1g}$, S $2p(2t_{1u})\rightarrow 2t_{2g}$, and S $2p(2t_{1u})\rightarrow 4e_g$] decrease relatively smoothly from a maximum value at or near to $K^2=0$. In contrast, the GOS curves for the dipole-forbidden transitions [S $2p(2t_{1u})\rightarrow 6t_{1u}$ excitation] extrapolate to a value close to zero. While the optical limit of the GOS for the 181-eV signal is statistically indistinguishable from 0, consistent with its absence in all reported photoabsorption spectra, the 177-eV signal has an extrapolated optical oscillator strength of 0.0085(8). While some part of this signal arises from unresolved Rydberg transitions [50], this contribution is relatively small, as can be seen from the high-resolution optical work [50]. Electron

TABLE III. Values of f_0, f_1, f_2, and f_3 derived from the modified Lassettre series analysis [Eq. (4)] for the S $2p$ excitation of SF_6 based on GOS values derived from peak areas and peak intensities. Numbers in square brackets indicate powers of 10.

	This work (peak areas)				This work [a]				Ying *et al.* [1] [a]			
State (UMO)	f_0	f_1/f_0	f_2/f_0	f_3/f_0	f_0	f_1/f_0	f_2/f_0	f_3/f_0	f_0	f_1/f_0	f_2/f_0	f_3/f_0
$T_{1u}(a_{1g})$	0.079	−88	3.37[3]	−4.29[4]	0.037	−101	4.73[3]	−7.03[4]	0.0327	−129.0	6.11[3]	−9.57[4]
A [b] (t_{1u})	0.0085	456	−2.72[4]	3.87[5]	0.0039	359	−1.74[4]	2.19[5]	0.0042	165.3	−3.78[3]	2.02[4]
B [b] (t_{1u})	0.0006	2946	−1.23[5]	1.57[6]	0.0012	1127	−4.30[4]	5.77[5]				
$T_{1u}(t_{2g})$	0.2253	−33	7.57[2]	−8.73[3]	0.108	−45	1.56[3]	−1.96[4]	0.103	−127.7	5.75[3]	−8.90[4]
$T_{1u}(e_g)$	0.2008	−37	1.14[3]	−2.36[4]	0.063	−59	2.64[3]	−4.15[4]	0.0653	−123.1	5.21[3]	−7.31[4]

[a] Based on peak intensities not peak areas.

[b] States are labeled A and B to reflect uncertainty in assignments [3].

energy-loss spectra recorded at higher resolution and similar K^2 [60] conclude that this region consists of four sharp Rydberg peaks overlapping the relatively broad S $2p \rightarrow 6t_{1u}$ transition [3]. Conversely, the similarity of the S $2p$ absorption spectra of solid and gaseous SF_6 [53] supports the view that the t_{1u} transition dominates this region. A nonzero intensity in the optical limit is consistent with the observations of Hudson *et al.* [50], who have attributed this signal to electronically forbidden but vibronically dipole-allowed transitions. It is interesting to note that the shapes of the 177-eV $A(t_{1u})$ and 181-eV $B(t_{1u})$ GOS curves are relatively similar, at least up to 13 a.u.$^{-2}$, with each one peaking at 3 a.u.$^{-2}$ (Fig. 6). This supports our suggestion [3] that these two states may have a common configurational origin.

B. Comparison to literature GOS values

Figures 5 and 6 contain comparisons of our results to those reported by Ying, Mathers, and Leung [1]. Clearly their results lie quite far below ours. A major factor is that Ying, Mathers, and Leung have chosen to report peak GOS values (in units of eV^{-1}) rather than integrated GOS values (which are unitless). Since peak intensities can be a strong function of spectral resolution, we have chosen to present GOS peak areas instead. Differences in both the normalization procedure and the approach used to derive GOS values can partially explain the differences between our GOS values and those of Ying, Mathers, and Leung [1]. In addition to the use of *intensity* not *area* measurements, the GOS curves of Ying, Mathers, and Leung were made absolute by single-point normalization to an absolute OOS value of 0.103 for the $2p \rightarrow 2t_{2g}$ transition derived from the photoabsorption work of Blechschmidt *et al.* [53]. It is not clear how this value was derived from Ref. [53]. Another possible factor could be differences in the procedure used to isolate the signal for the $T_{1u}(\mathrm{S}\ 2p^{-1},t_{2g})$ and $T_{1u}(\mathrm{S}\ 2p^{-1},e_g)$ electronic states from the underlying valence and S $2p$ continua. Ying, Mathers, and Leung [1] carried out a subtraction of the non-S $2p$ background that allowed them to analyze their data between 182 and 200 eV without any continuum contribution. A further concern is that Ying, Mathers, and Leung did not make a correction for the angle dependence of the size of the interaction region, a factor we have taken into account by measurement and subtraction of the nonjet signal. The sense of the deviation between the two sets of results—a reduction in intensity at large K^2—is exactly the result if the analysis is carried out without correcting for the nonjet signal. While the nonjet signal appears preferentially at small scattering angles, the effect on the GOS is a suppression of the large-K^2 data and not an enhancement of the small-K^2 data, since the GOS is normalized at the optical limit.

To better understand how each of the above factors can affect the GOS values for the t_{2g} and e_g features, we have

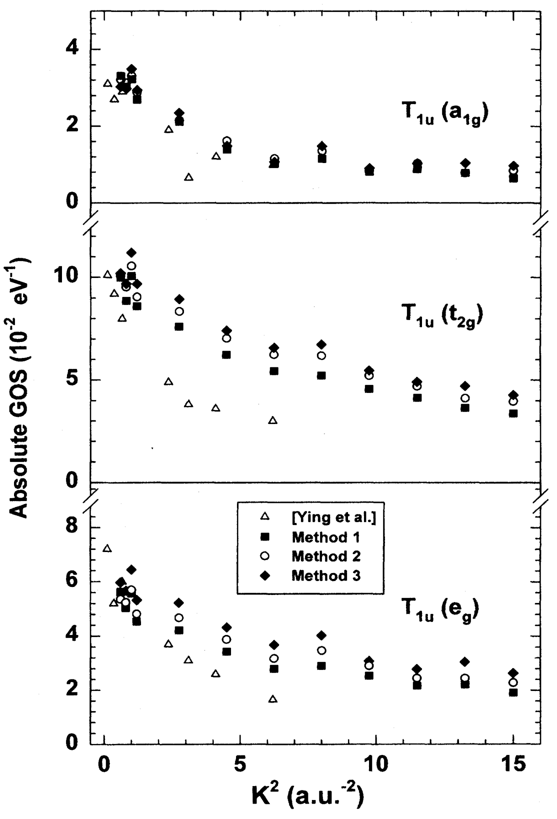

FIG. 7. GOS curves for the $T_{1u}(a_{1g})$, $T_{1u}(t_{2g})$, and $T_{1u}(e_g)$ dipole-coupled S $2p$ excited states derived from our experimental *intensity* data as described in the text (methods 1, 2, and 3) compared to the *intensity-based* GOS values (indicated by open triangles) reported by Ying, Mathers, and Leung [1]. These three separate methods of analysis test the origin of the differences between our results and those of Ying, Mathers, and Leung (see the text for details). Note that the vertical scales in this plot are much smaller than those in Fig. 5 since they are GOS values based on peak intensities, not peak areas.

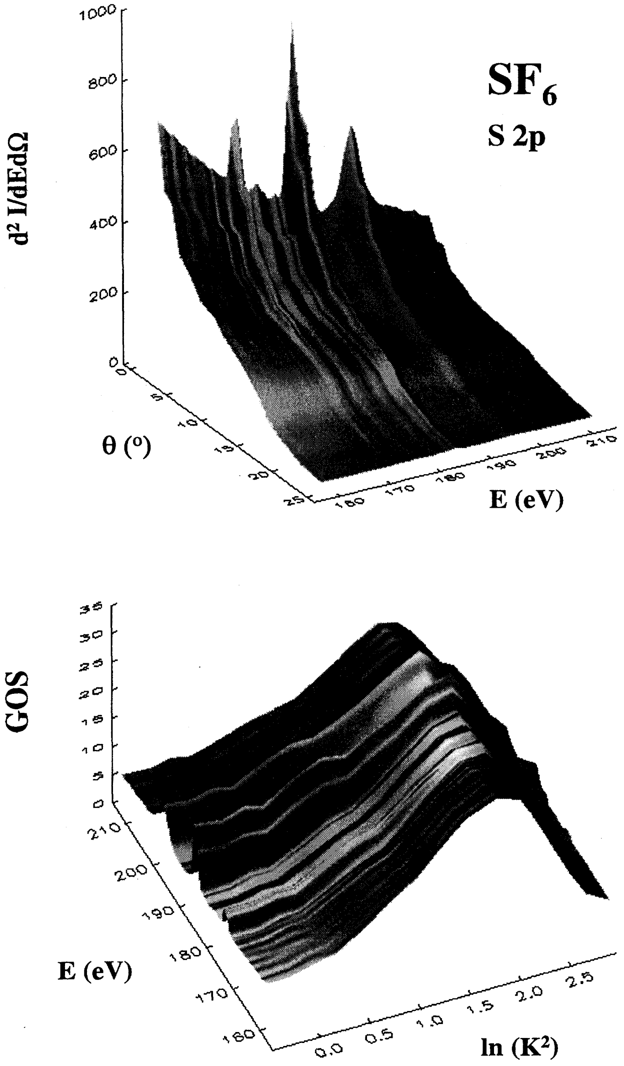

FIG. 8. Surface of relative inelastic electron scattering cross sections for SF_6 in the S $2p$ region. (b) Bethe surface for SF_6 in the region of S $2p$ excitation derived from the energy-loss measurements as described in the text.

carried out analyses based on the *peak intensities* of our data in several ways, including a method matched as closely as possible to that reported by Ying, Mathers, and Leung. Figure 7 plots the results reported by Ying, Mathers, and Leung [1] in comparison to our values derived from *method 1*, the same procedure employed by Ying, Mathers, and Leung [1] [no continua contribution for the S $2p$ signal, no correction for the nonjet background signal, and the same scale factor (N) for converting relative to absolute GOS scales]; *method 2*, the same procedure as method 1 but with correction for the nonjet background signal; and *method* 3, our optimized procedure carried out on peak intensities.

For the $T_{1u}(a_{1g})$ and $T_{1u}(e_g)$ signals (Fig. 7), as well as the $T_{2g}(t_{1u})$ signal (not shown), the recipe closest to that of Ying, Mathers, and Leung (method 1) gives results that agree within the mutual experimental error bars. However, very large residual discrepancies are found for the t_{2g} signal. The intensity-based GOS derived from our results is much lower than the value reported by Ying, Mathers, and Leung [1], except at the minimum momentum transfer where the results are forced to be approximately the same by the normalization procedures used. We believe that this may be due to the better resolution employed in our work since the GOS values of Fig. 7 are estimated from peak intensities, not peak areas, and thus the values are resolution dependent. Note that resolution is *not* a factor with regard to accuracy of the GOS reported in Figs. 5 and 6 since these are derived from peak areas, which are independent of resolution.

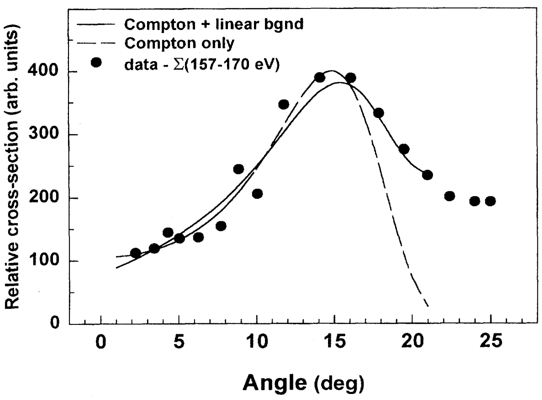

FIG. 9. Comparison of experimental valence "Compton profile," the intensity of valence ionization signal integrated between 157 and 170 eV as a function of scattering angle, with predictions based on (i) only the binary encounter Compton formula [29] (dashed line) and (ii) the Compton formula plus a linear background (solid line).

When the nonjet background correction is applied (method 2) the effect is exactly that mentioned, i.e., large discrepancies between our values and Ying, Mathers, and Leung's [1] for large K^2. Poor agreement is found when the GOS determination is carried out with our procedure (method 3) where the continua steps, nonjet signal, and a different scale factor N were all included. The results show that the correction for the angle dependence of the scattering volume (by subtraction of the nonjet signal) is a critical step of the data analysis procedure. The results can be very sensitive to the way this correction is performed.

C. Bethe surface and valence Compton scattering

The three-dimensional representation of the GOS over extended ranges of energy-loss and momentum transfer (GOS as a function of $\ln K_2$ and energy loss) gives a surface, named the Bethe surface by Inokuti [5]. In principle, Bethe surfaces contain the information necessary to predict the behavior of the species under charge-particle impact under all conditions where the first Born approximation holds. The electron energy-loss spectra of SF_6 were converted to absolute GOS curves, after Bethe-Born correction at each energy loss [using Eq. (1)] and normalization with OOS values taken from the literature as explained in previous sections. Because the momentum transfer varies within each recorded spectrum, a variable kinematic conversion was used for each data file.

Figure 8(a) plots the relative inelastic cross section as a function of angle and energy loss for SF_6 in the S $2p$ region.

The cross section drops rapidly with increasing scattering angle, largely because of the kinematic term. This makes nondipole core-excitation studies a considerable experimental challenge. Figure 8(b) presents the Bethe surface of SF_6 derived from these results. It is rotated 90° relative to the cross-section plot in order to better reveal the S $2p$ excitation features that are superimposed on a large valence ionization background. Within the uncertainties in absolute values (perhaps 30%, largely associated with the poorly known optical values), this plot is accurate aside from not taking into account small variations in the K^2 value within each spectrum, which should place our fixed-angle curves at a small angle relative to the fixed-K^2 planes on which they are plotted. A comparison of Figs. 8(a) and 8(b) indicates the large role the Bethe-Born kinematic factor plays in determining the overall shape of the GOS.

The broad maximum peaking around 8 a.u.$^{-2}$ [$\ln(K^2)$ of ~ 2] is the Bethe ridge which is associated with Compton scattering of the incident electron by the valence electrons of SF_6 [5]. It is also apparent in the cross-section plot, but only as a broad shoulder for scattering angles between 12° and 20°. In order to confirm this explanation for the dramatic difference between Figs. 8(a) and 8(b), we have evaluated the integrated valence-shell ionization signal in the GOS curve for energy losses between 157 and 170 eV and compared its shape to a functional form based on the Compton effect [29] (Fig. 9). While the curve based solely on the Compton scattering signal gives a reasonable fit up to 15°, the addition of a linear background to the fit gives much better agreement with experiment. The intent of this aspect of our analysis is to demonstrate the physical origin of the dominant maximum in the GOS rather than derive average valence momentum functions. As stressed by Letardi, Camilloni, and Stefani [29], the valence Compton component (Bethe ridge) can be a major concern in quantitative evaluation of core excitation spectra.

IV. SUMMARY

The generalized oscillator strengths for S $2p$ excitations in SF_6 have been derived in the region $0<K^2<20$ a.u.$^{-2}$. The procedure used to obtain these results have been presented in detail and their performance evaluated by comparison to literature GOSs for S $2p$ excitation of SF_6. The Bethe surface of S $2p$ excited SF_6 has been derived.

ACKNOWLEDGMENTS

This research is supported by NSERC (Canada). J.T.F. thanks NSERC for financial support. C.C.T. thanks CNPq (Brazil) for financial support.

---

[1] J. F. Ying, C. P. Mathers, and K. T. Leung, Phys. Rev. A **47**, R5 (1993).
[2] A. P. Hitchcock and D. C. Mancini, J. Electron Spectrosc. **67**, 1 (1994).
[3] J. T. Francis, C. C. Turci, T. Tyliszczak, G. G. B. de Souza, and A. P. Hitchcock, preceding paper, Phys. Rev. A **52**, 4665 (1995).
[4] H. Bethe, Ann. Phys. (Leipzig) **5**, 325 (1930).
[5] M. Inokuti, Rev. Mod. Phys. **43**, 297 (1971).
[6] C. E. Brion, Comments At. Mol. Phys. **16**, 249 (1985).
[7] W. F. Chan, G. Cooper, and C. E. Brion, Phys. Rev. A **44**, 186 (1991).
[8] W. F. Chan, G. Cooper, X. Guo, and C. E. Brion, Phys. Rev. A **45**, 1420 (1992).
[9] W. F. Chan, G. Cooper, X. Guo, G. R. Burton, and C. E. Brion, Phys. Rev. A **46**, 149 (1992).
[10] E. N. Lassettre, J. Chem. Phys. **43**, 4479 (1965).
[11] M. A. Dillon and E. N. Lassettre, J. Chem. Phys. **62**, 2373 (1975).
[12] E. N. Lassettre and A. Skerbele, J. Chem. Phys. **54**, 1597 (1971).
[13] W. R. Harshbarger, A. Skerbele, and E. N. Lassettre, J. Chem. Phys. **54**, 3784 (1971).
[14] A. Z. Msezane and I. A. Sakmar, Phys. Rev. A **49**, 2405 (1994).
[15] J. S. Lee, T. C. Wong, and R. A. Bonham, J. Chem. Phys. **63**, 1643 (1975).
[16] J. S. Lee, J. Chem. Phys. **67**, 3998 (1977).
[17] A. C. de A. e. Souza and G. G. B. de Souza, Phys. Rev. A **38**, 4488 (1988).
[18] K. N. Klump and E. N. Lassettre, Chem. Phys. Lett. **51**, 99 (1977).
[19] K. N. Klump and E. N. Lassettre, J. Chem. Phys. **68**, 3511 (1978).
[20] J. F. Ying, C. P. Mathers, K. T. Leung, H. P. Pritchard, C. Winstead, and V. McKoy, Chem. Phys. Lett. **212**, 289 (1993).
[21] J. T. Francis, C. Enkvist, S. Lunell, and A. P. Hitchcock, Can. J. Phys. **72**, 879 (1994); J. T. Francis, N. Kosugi, and A. P. Hitchcock, J. Chem. Phys. **101**, 10 429 (1994).
[22] R. A. Bonham, J. Chem. Phys. **36**, 3260 (1962).
[23] Y.-K. Kim, M. Inokuti, G. E. Chamberlain, and S. R. Mielczarek, Phys. Rev. Lett. **21**, 1146 (1968).
[24] K. J. Miller, J. Chem. Phys. **62**, 1759 (1975).
[25] M. Krauss and S. R. Mielczarek, J. Chem. Phys. **51**, 5241 (1969).
[26] K. J. Miller, S. R. Mielczarek, and M. Krauss, J. Chem. Phys. **51**, 26 (1969).
[27] J. F. Ying and K. T. Leung, J. Chem. Phys. **100**, 1011 (1994).
[28] R. S. Barbieri and R. A. Bonham, Phys. Rev. A **45**, 7929 (1992).
[29] P. Letardi, R. Camilloni, and G. Stefani, Phys. Rev. B **40**, 3311 (1989).
[30] H. F. Wellenstein, R. A. Bonham, and R. C. Ulsh, Phys. Rev. A **8**, 304 (1973).
[31] A. Lahmam-Bennani, A. Duguet, H. F. Wellenstein, and M. Rouault, J. Chem. Phys. **72**, 6398 (1980).
[32] R. A. Bonham and H. F. Wellenstein, in *Compton Scattering*, edited by B. Williams (McGraw-Hill, New York, 1977), Chap. 8.
[33] J. F. Ying and K. T. Leung, J. Chem. Phys. **101**, 8333 (1994).
[34] A. Skerbele and E. N. Lassettre, J. Chem. Phys. **52**, 2708 (1970).
[35] F. Hanne and J. Kessler, Phys. Rev. A **5**, 2457 (1972).
[36] T. C. Wong, J. S. Lee, and R. A. Bonham, Phys. Rev. A **11**, 1963 (1975).

[37] C. E. Bielschowsky, G. G. B. de Souza, C. A. Lucas, and H. M. Boechat Roberty, Phys. Rev. A **38**, 3405 (1988).

[38] J. F. Ying, T. A. Daniels, C. P. Mathers, H. Zhu, and K. T. Leung, J. Chem. Phys. **99**, 3390 (1993).

[39] J. F. Ying and K. T. Leung, J. Chem. Phys. **100**, 7120 (1994).

[40] H. M. Boechat Roberty and G. G. B. de Souza, J. Phys. B **25**, 4641 (1992).

[41] R. Camilloni, E. Fainelli, G. Petrocelli, and G. Stefani, J. Phys. B **20**, 1839 (1987).

[42] H. M. Boechat Roberty, C. E. Bielschowsky, and G. G. B. de Souza, Phys. Rev. A **44**, 1694 (1991).

[43] M. P. de Miranda, C. E. Bielschowsky, H. M. Boechat Roberty, and G. G. B. de Souza, Phys. Rev. A **49**, 2399 (1994).

[44] D. A. Shaw, G. C. King, F. H. Read, and D. Cvejanovic, J. Phys. B **15**, 1785 (1982).

[45] J. F. Ying and K. T. Leung, J. Chem. Phys. **101**, 7311 (1994).

[46] J. T. Francis, T. Tyliszczak, and A. P. Hitchcock (unpublished).

[47] J. P. Bromberg, J. Chem. Phys. **50**, 3906 (1968).

[48] E. N. Lassettre, A. Skerbele, and M. A. Dillon, J. Chem. Phys. **50**, 1829 (1969).

[49] A. P. Hitchcock, T. Tyliszczak, P. Aebi, X. H. Feng, Z. H. Lu, J.-M. Baribeau, and T. E. Jackman, Surf. Sci. **301**, 260 (1994).

[50] E. Hudson, D. A. Shirley, M. Domke, G. Remmers, A. Puschmann, T. Mandel, C. Xue, and G. Kaindl, Phys. Rev. A **47**, 361 (1993).

[51] J. Stöhr, *NEXAFS Spectroscopy*, Springer Series in Surface Sciences Vol. 25 (Springer-Verlag, Heidelberg, 1992).

[52] J. L. Dehmer, J. Chem. Phys. **56**, 4496 (1972).

[53] D. Blechschmidt, R. Haensel, E. E. Koch, U. Nielsen, and T. Sagawa, Chem. Phys. Lett. **14**, 33 (1972).

[54] B. M. Addison-Jones, K. H. Tan, G. M. Bancroft, and F. Cerrina, Chem. Phys. Lett. **129**, 468 (1986).

[55] L. Vriens, Phys. Rev. **160**, 100 (1967).

[56] W. L. Jolly, K. D. Bomben, and C. J. Eyermann, At. Data Nucl. Data Tables **31**, 433 (1984).

[57] R. W. Shaw, Jr., T. X. Caroll, and T. D. Thomas, J. Am. Chem. Soc. **95**, 5870 (1973).

[58] W. M. Huo, J. Chem. Phys. **71**, 1593 (1979).

[59] K. N. Klump and E. N. Lassettre, Can. J. Phys. **53**, 1825 (1975).

[60] A. P. Hitchcock and C. E. Brion, Chem. Phys. **33**, 55 (1978).

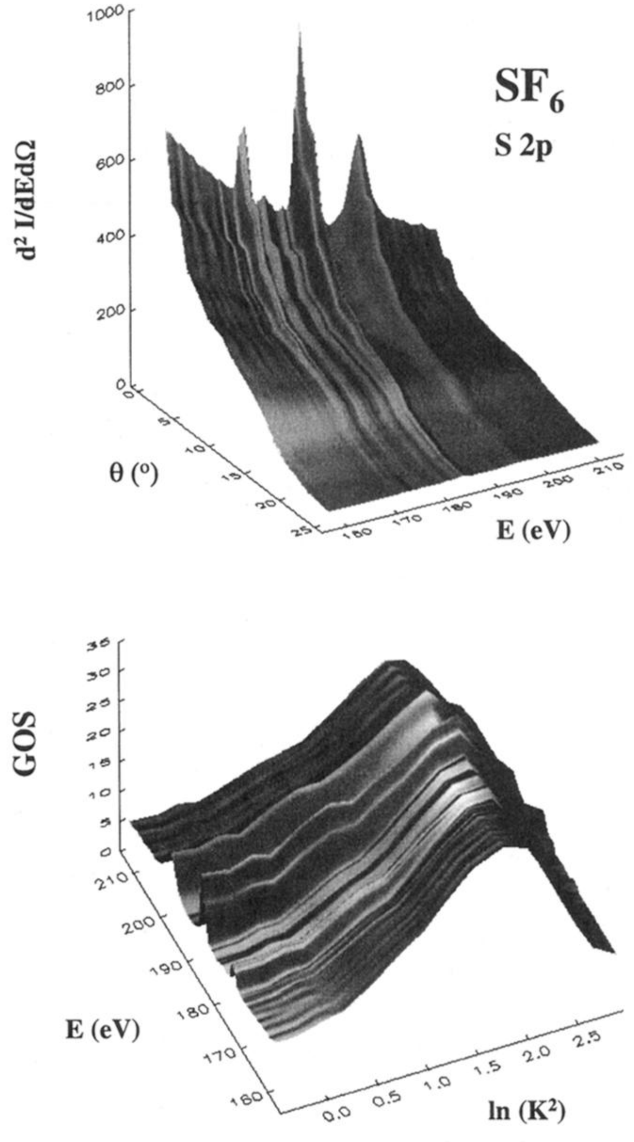

FIG. 8. Surface of relative inelastic electron scattering cross sections for SF_6 in the S 2*p* region. (b) Bethe surface for SF_6 in the region of S 2*p* excitation derived from the energy-loss measurements as described in the text.